Solar Energy Materials & Solar Cells 224 (2021) 110995

Contents lists available at ScienceDirect

Solar Energy Materials and Solar Cells

journal homepage: http://www.elsevier.com/locate/solmat

Solar selective reflector materials: Another option for enhancing the efficiency of the high-temperature solar receivers/reactors

Wujun Wang [a,*], Wangzhong Mu [b], Fei Ye [c], Silvia Trevisan [a], Joydeep Dutta [c], Björn Laumert [a]

[a] Department of Energy Technology, KTH Royal Institute of Technology, Brinellvägen 68, 100 44, Stockholm, Sweden
[b] Department of Material Science and Engineering, KTH Royal Institute of Technology, Brinellvägen 23, 100 44, Stockholm, Sweden
[c] Department of Applied Physics, KTH Royal Institute of Technology, Hannes Alfvensväg 12, 114 19, Stockholm, Sweden

ARTICLE INFO

Keywords:
Solar selective reflector
Cavity receiver
Metallic oxide coating
Spectral hemispherical absorptivity
Concentrating solar power

ABSTRACT

The cavity wall is an important part of a cavity receiver in determining the receiver efficiency. Using solar selective reflector (SSR) materials with low solar absorptivity and high thermal emissivity for the cavity wall design is one efficient way to improve the receiver efficiency. In this work, we present a systematic study of the optical and high-temperature stability performances of six different SSR materials: one refractory ceramic fiber based substrate material (Fiberfrax 140) and five metallic oxide coatings which are prepared by mixing metallic oxide powders of alumina, magnesium oxide and titanium dioxide with commercial inorganic adhesives. The thermal stability was studied by heating up and keeping the six candidate materials in atmospheric conditions at a temperature of 1250 °C for 200 h. The spectrum of hemispherical reflectance in the spectrum band 0.25–25 μm was measured for analyzing the optical performance of the candidate materials. The obtained results show that all the six materials studied have good solar selective reflection characteristics, i.e, low solar absorptivity and relatively high thermal emissivity. Especially, the alumina coated substrate material shows excellent performances both for thermal stability and solar selective reflection. The solar reflectivity can reach 94.6%.

1. Introduction

Concentrating solar power (CSP) technology, which converts the unlimited solar radiation into heat for electric power generation through different thermal power cycles, is considered to be one of the most promising pathways to the future fossil fuel free society [1,2]. In CSP systems, the receiver, where the solar irradiation is absorbed and converted into heat, is always the most critical component and often the bottleneck for limited system efficiency [3]. Energy loss at the receiver is inevitable, and it increases significantly with the increase of receiver temperature. However, the receiver acts as the heat source for the thermal power cycle, and its outlet temperature directly limits the theoretical efficiency of the power cycle according to the second law of thermodynamics [4]. Therefore, developing receivers with higher efficiency and working at higher temperatures is an important way for enhancing the competitiveness of CSP technologies in commercial applications [5].

Designing the absorber in a cavity shape is one of the main strategies for modern high-efficiency point-focusing receiver designs, especially for solar Brayton systems and solar thermochemical applications that require relatively high working temperatures [6–8]. Cavity receivers are usually designed as opaque heat exchangers, where the concentrated solar irradiation is absorbed and transferred to the working fluid by conduction through the absorber wall and convection of the working fluid [9,10]. By using the 'cavity effect' (high absorptivity are achieved by multiple reflections inside the cavity), cavity receivers can achieve higher efficiencies and outlet working fluid temperatures than those receivers with flat absorbers [11]. In view of the energy flow, the modern cavity receiver designs can be classified into two groups: direct absorption receiver and partially indirect absorption receiver, as schematically represented in Fig. 1. For a direct absorption receiver, the concentrated solar irradiation is absorbed directly by the absorber like in radial type impinging receivers [12]. In direct absorption cavity receivers, the absorbers are the most critical components that usually need to sustain high light fluxes, high temperatures and high pressures over a long period. At the moment, Nickel-based superalloys are widely used as the absorber material in large-scale commercial direct absorption receivers which are usually designed based on modular tubular bundle structure. Due to the limitation of the allowable working temperatures for these Nickel-based superalloys, it is difficult to achieve an outlet working fluid temperature above 900 °C [13]. In order to obtain higher

* Corresponding author.
E-mail addresses: wujun@kth.se, wujun.wang@energy.kth.se (W. Wang).

https://doi.org/10.1016/j.solmat.2021.110995
Received 4 September 2020; Received in revised form 29 January 2021; Accepted 2 February 2021
Available online 11 February 2021

Nomenclature

E	spectral emissive power, W/(m^2·nm)
I	spectral solar direct normal irradiation, W/(m^2·nm)
T	temperature, K
Greek	
α	absorptivity
ε	emissivity
λ	wavelength, μm
ρ	reflectivity
Subscripts	
b	blackbody
sol	solar irradiation
Abbreviations	
CSP	concentrated solar power
SEM	scanning electron microscopy
SSA	solar selective absorber material
SSR	solar selective reflector material
XRD	X-ray diffraction

outlet temperature, ceramic materials, e.g. silica carbide ceramic, are also used in lab- or pilot-scale high-temperature direct absorption receivers [14]. However, these ceramic materials are usually very expensive and difficult to manufacture in large-sizes [15]. Thus, the high-temperature (working fluid temperature >800 °C) direct absorption receivers are so far only designed for less than 1 MW small-scale applications.

Unlike the direct absorption receivers, the radiation energy from the concentrated solar irradiation is reflected or re-radiated by the cavity wall before arriving at the absorber in a partially indirect absorption receiver, such as tubular cavity receivers [16,17]. In these partially indirect absorption cavity receivers, the absorber can be designed in arrays of smaller units to minimize the usage of the expensive refractory materials and to maximize the mechanical performances of the absorber. Therefore, the partially indirect absorption cavity receivers are more suitable for large-scale CSP or solar thermochemical applications. In general, the possible energy losses of a cavity receiver are caused by back-reflection, thermal radiation and convection through the aperture, as well as the heat conduction through the cavity material. With the help of the 'cavity effect', a well-designed cavity receiver can be considered as an approximate blackbody of approximately the size of its aperture, and thus the optical efficiency of a cavity receiver can easily reach above 95% [18]. Thus, the main energy losses of a well-insulated cavity receiver can be mainly attributed to thermal radiation and natural convection heat losses through the aperture that are directly related to the cavity wall temperature [19–21]. Thus, controlling the cavity wall temperature at a relatively low level is not only useful in reducing the technical requirements for the high-temperature mechanical performances of the candidate materials, but also is an efficient way towards enhancing the efficiency of partially indirect absorption receivers.

Considering the energy balance on the cavity wall, as shown in Fig. 1 (B), the main energy input is the absorbed solar flux (including the multi-reflection losses), and the outputs are in the form of thermal radiation and heat convection. Thus, the main strategies for controlling the cavity wall temperature can be achieved by minimizing the absorption of the solar flux as well as by maximizing the thermal radiation. Both phenomena's are governed by electromagnetic energy transfer but occur at different spectral bands [22,23]. Thus, it is of interest to investigate the potential of using solar selective material for controlling the cavity wall temperature. Unlike the traditional widely used solar selective absorber (SSA) materials [24], the candidate solar selective materials are preferred to have lower solar absorptivity and higher thermal emissivity for cavity wall applications. Herein, we denominate such materials with a new name as solar selective reflector (SSR) material. During the past decades, numerous studies have been reported on SSA materials for improving receiver efficiencies [25–27], but the SSR materials still have not received sufficient attention in the published literature. With increasing requirements for the design of high-temperature point-focusing receivers and reactors, research on the SSR materials is attracting more attention. Based on the operating experiences of a tubular cavity receiver with ceramic fiber fabric cavity wall, Ebert et al. conclude that better receiver performance can be achieved by applying surface treatment on the cavity wall materials [28]. Recently, Garrido et al. have found that the thermal emissivity (ε) and the solar absorptivity (α) of the cavity wall has a strong influence on the efficiency of a cavity receiver for solar Stirling system [29]. The results show that, when the cavity temperature is higher than the absorber temperature, a high ε/α value leads to a positive impact in the

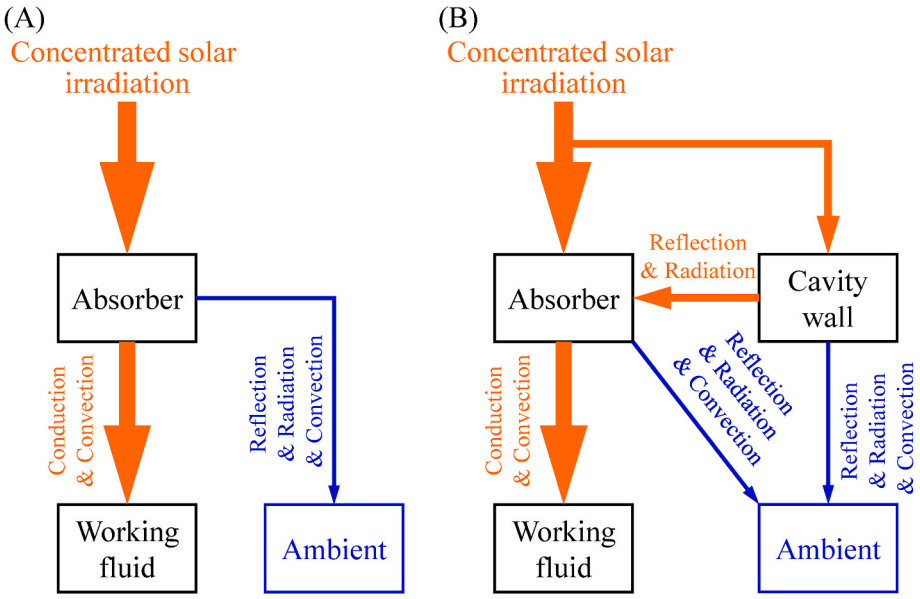

Fig. 1. Schematic representation of two types of cavity receivers: (A) direct absorption receiver and (B) partially indirect absorption receiver.

efficiency; when the cavity temperature is low, lower values of both ε and α are helpful for improving receiver efficiencies.

In this work, we studied the performance of six different SSR materials: refractory ceramic fiber-based substrate material and five metallic oxide coatings prepared by mixing metallic oxide powders of alumina (Al_2O_3), magnesium oxide (MgO) and titanium dioxide (TiO_2) with commercial inorganic adhesives coated on the substrate material. Thermal stability tests were conducted in atmospheric conditions at a temperature of 1250 °C for 200 h. The optical performance is studied by analyzing the spectral hemispherical reflectance in the spectrum band 0.25–25 μm Al_2O_3 amongst the six candidate material coatings show the best solar selective reflection characteristics.

2. Experimental details

2.1. Material selection and coating preparation

In order to minimize the conduction heat loss through the cavity wall, a material with good insulation properties is preferred for the cavity wall. Fiberfrax 140 is an alumina-zirconia silica based refractory ceramic fiber material that is widely used in the large-scale high-temperature receivers of power tower systems and in industrial furnaces [30]. It has excellent insulating properties, high temperature thermal stability, and manufacturability rendering it as an ideal material for manufacturing cavity walls [29]. In this study, Fiberfrax 140 is used as a reference for evaluating the performances of the SSR materials. In the published literature, Al_2O_3, MgO and TiO_2 are known to be good refractory materials with relatively high solar reflectivity and thermal stability [31]. In general, simple application and low cost are two of the most important factors in determining whether a technology can be commercialized in the future. Therefore, in this study, these potential SSR materials are prepared in the form of powder, and directly painted on Fiberfrax 140 substrate samples (with same size of 30 × 30 × 10 mm) using a brush upon mixing with commercial refractory inorganic adhesives. Different samples are obtained by changing the material compositions and weight ratios. After drying the samples, careful curing was carried out following the specifications of the commercial inorganic adhesives. The thicknesses of the coatings are measured that within the range of 0.8–1.5 mm. In order to select most stable coatings and maximizing the performance of the commercial inorganic adhesives, the samples are cured or preliminarily tested in open atmosphere at a temperature of 1000 °C for 24 h in a chamber furnace (Nabertherm®). Finally, the substrate sample and the other five coatings with good quality were subjected to further high-temperature thermal stability studies at 1250 °C for 200 h. The detailed information of the selected samples is shown in Table 1. A high temperature tube furnace (Entech type) is used for this test. Prior to the test, the hot zone in the horizontal tube furnace was calibrated by K-type thermocouples to ensure the thermal stability test was conducted at the desired temperature range (1250 ± 10 °C). During the testing, the samples are supported by two alumina ceramic rods to keep the coating surfaces horizontally in the center of the tube furnace. Coating color change, surface micro crack generation, and sample deformation are selected as the main criterions for evaluating the thermal stability performance of the candidate materials at this testing stage.

Table 1
Details of the sample preparation conditions used in this work.

Sample name	Material composition	Weight ratio	Adhesive	Cure condition
Substrate	Fiberfrax 140	N/A	N/A	N/A
Coating 1	100% Al_2O_3	N/A	Pyro-Paint™ 634-AL	Dry at room temperature and post cure at 100 °C
Coating 2	MgO + Al_2O_3	1:1	Resbond™ 906	Dry at room temperature and post cure at 120 °C
Coating 3	MgO + Al_2O_3	2:1	Resbond™ 906	Dry at room temperature and post cure at 120 °C
Coating 4	100% MgO	N/A	Resbond™ 906	Dry at room temperature and post cure at 120 °C
Coating 5	MgO + TiO_2	7:1	Resbond™ 906	Dry at room temperature and post cure at 120 °C

2.2. Material characterizations and optical measurements

The crystal structure and phase composition of coating materials were obtained from X-ray diffraction (XRD) patterns obtained from Empyrean S2 diffractometers (PANalytical, Netherlands) using Cu Kα radiation (λ = 0.154 nm) and scanning in the 2θ range of 15°–70°.

The spectrum of hemispherical reflectance from 0.25 to 2.5 μm was measured with a laboratory two-beam scan spectrophotometer (PerkinElmer Lambda 950) equipped with an Integrating Sphere of 150 mm diameter. Two light sources (halogen and deuterium lamp) and two detectors (photodiode and InGaAs) contribute to the sensibility over the entire spectrum. The measurements are referenced with a calibrated standard (Spectralon 99%). The spectrum of hemispherical reflectance from 1.5 μm to 25 μm is measured with a reflectometer (Surface Optics Corporation SOC-100 HDR) and a spectrophotometer (Nicolet FTIR 6700). The SOC-100 is equipped with 2π imaging hemi ellipsoid (gold coated) to illuminate the sample from all directions using a 700 °C blackbody source. A movable mirror collects the reflected collimated light and directs it to the FTIR to obtain the reflectance spectrum. A gold plated calibrated specular or diffuse reflectance standard is used as the reference during the measurement. Usually, the SOC 100 is much more reliable than the PerkinElmer Lambda 950 for the wavelength over 2 μm. Therefore, considering the accuracy differences, discontinuity might happen for the hemispherical reflectance results at the wavelength of 2 μm.

A light optical microscope (LOM, Leica DMR) and scanning electron microscopy (SEM, GEMINI Ultra 55, Carl Zeiss, Oberkochen, Germany) were used to characterize the surface morphology of the samples after thermal stability test at 1250 °C for 200 h.

2.3. Energy analysis

Considering all the samples are opaque gray bodies, according to Kirchhoff's law, the spectral absorptivity/emissivity distributions of the investigated samples can be obtained by Eq. (1) [32].

$$\alpha(\lambda) = \varepsilon(\lambda) = 1 - \rho(\lambda) \tag{1}$$

where λ is the wavelength, $\alpha(\lambda)$ is the spectral absorptivity, $\varepsilon(\lambda)$ is the spectral emissivity and $\rho(\lambda)$ is the spectral reflectivity. The normal solar absorptivity α_{sol} and the normal thermal emissivity $\varepsilon(T)$ were calculated from the reflectance measurements using the following equations [33]:

$$\alpha_{sol} = \frac{\int_{280nm}^{2500nm} I_{sol}(\lambda)(1-\rho(\lambda))d\lambda}{\int_{280nm}^{2500nm} I_{sol}(\lambda)d\lambda} \tag{2}$$

$$\varepsilon(T) = \frac{\int_{280nm}^{25000nm} E_b(\lambda,T)(1-\rho(\lambda))d\lambda}{\int_{280nm}^{25000nm} E_b(\lambda,T)d\lambda} \tag{3}$$

where T is the surface temperature, $E_b(\lambda, T)$ is the blackbody spectral emissive power, $I_{sol}(\lambda)$ is the ASTM standard AM 1.5 direct normal terrestrial solar irradiance [34]. Considering that these coatings are expected to work above 800 °C, the blackbody spectral emissive power at 25,000 nm is less than 0.3% of its peak value at 2700 nm according to Stefan-Boltzmann Law. Therefore, the wavelength range 280–25000 nm is broad enough for the temperature range in this study.

3. Results and discussion

3.1. Visual inspection

Since all the substrate and coating materials are inorganic oxides, chemical stabilities of these materials are good. However, due to the high temperature and oxidizing environment crystal structure of the materials could be affected. Hence, all the samples were first tested in open atmosphere at a temperature of 1000 °C for 24 h for visual inspection. Though the colors of the coatings are all white after painting and curing, slight color changes could observed after the preliminary testing. Following the thermal stability testing at 1250 °C for 200 h in ambient atmosphere and pressure with an airflow of 0.02 m/s, color of the samples was examined as shown in Fig. 2. Only the colors of the 100% Al_2O_3 sample (Coating 1) and the Fiberfrax 140 sample (Substrate material) were not affected, while slight color changes could be observed in the other samples. Furthermore, since all these SSR coating materials are brittle ceramics, the thermal stress will also be an important factor that could lead to cracking or chipping of the coatings. In the six samples studied here, significant cracks are observed in the Coating 5. By comparing the sample shapes before and after exposure to high temperature, clear deformation can be observed in Coating 3 and 4. Especially deformation of Coating 4 is significant. Thus, Coatings 3, 4 and 5 are not very suitable for potential real world applications. Considering the compositions of these coatings, MgO seems to be disadvantageous for maintaining the thermal mechanical stability of the coating. From mechanical point of view, 100% Al_2O_3 is the best coating candidate for Fiberfrax 140 substrate coating in real world applications.

3.2. XRD study

The crystal structure and phase composition of all coatings examined by XRD is shown in Fig. 3. Coating 1 shows a pure hexagonal crystal structure with chemical formula of Al_2O_3, which matches well with the ICDD (International Center for Diffraction Data) powder diffraction file 98-016-0605 with the most intense peaks from (104), (113), and (116) planes. Since coating 1 was prepared by mixing Al_2O_3 powder with Pyro-Paint 634-AL adhesive, and the adhesive mainly contains alumina filler the same composition as the SSR material in this coating, only a single crystalline phase (Al_2O_3) was detected by XRD. For other four coatings, MgO is the major composition, therefore, a magnesia-based adhesive

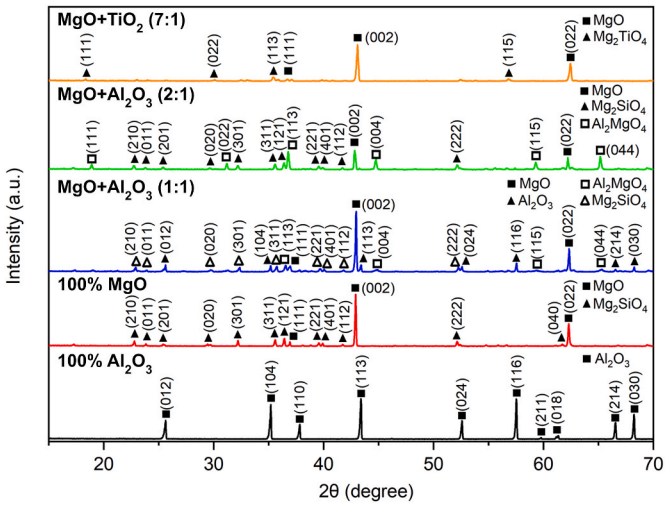

Fig. 3. XRD patterns of the coatings prepared from Al_2O_3, MgO–Al_2O_3 (1:1), MgO–Al_2O_3 (2:1), MgO, and MgO–TiO_2 (7:1) on Fiberfrax 140 substrate.

Resbond 906 was used in order to obtain a well-formed coating. For coating 2, prepared using MgO and Al_2O_3 in 1:1 ratio, the most intense peaks at 2θ values of 42.9° and 62.3° that can be indexed as (002) and (022) planes of MgO with cubic structure (ICDD file: 98-008-8058) is observed along with other diffraction peaks corresponding to (012), (104), (113), (024), (116), (214), and (030) crystal planes of Al_2O_3. Apart from the pristine phases of MgO and Al_2O_3, two composite phases are also identified, i.e., Al_2MgO_4 and Mg_2SiO_4. Al_2MgO_4, an alloy formed from reaction between MgO and Al_2O_3, with a cubic spinel structure. Another composite phase of Mg_2SiO_4 is observed where the silicate from the substrate material of Fiberfrax 140 reacts with alumina. Diffraction peaks at 2θ of 22.7°, 23.7°, 29.7°, 32.1°, 35.5°, 39.5°, 39.8°, 41.6°, 52.0° corresponding to (210), (011), (020), (301), (311), (221), (401), (112), (222) planes of Mg_2SiO_4 with orthorhombic structure according to ICDD file 98-006-4738 are also observed. When the amount of MgO was increased to 2:1 ratio in MgO–Al_2O_3 mixture (coating 3), a pure phase of Al_2O_3 is not observed, thus suggesting complete consumption of Al_2O_3 during the formation of Al_2MgO_4 phase. However, excess MgO remains in its pristine form as is evidenced from the diffraction peaks at 42.9° and 62.3° corresponding to its (002) and (022) crystal planes. Mg_2SiO_4 and Al_2MgO_4 can also be identified similar to what was observed in samples prepared with 1:1 ratio of MgO and Al_2O_3. However, since no pristine Al_2O_3 phase is observed in coating prepared from MgO and Al_2O_3 in 2:1 ratio, the formed Al_2MgO_4 has a relatively stronger intensity than that of Mg_2SiO_4, which is different from the coating prepared from MgO and Al_2O_3 in 1:1 ratio. In case of coating 4 prepared using MgO only, besides the phase of MgO, diffraction peaks of Mg_2SiO_4 are observed, indicating higher chemical

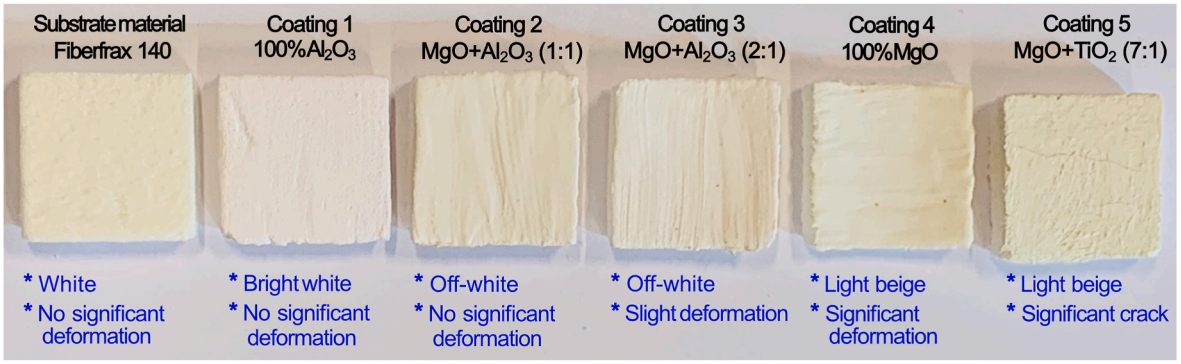

Fig. 2. Photos for the coatings after exposing at a temperature of 1250 °C and an ambient pressure with an air flow of 0.02 m/s for 200 h.

reactivity of MgO than Al_2O_3 in reaction with substrate material. In coating 5 prepared from MgO and TiO_2 in ratio of 7:1, MgO is obviously the major phase with no noticeable diffraction from TiO_2. Instead, due to the high reactivity of MgO, Mg_2TiO_4 with a cubic structure could be found as depicted from the diffraction peaks at 18.2°, 29.9°, 35.2°, 56.6° corresponding to the (111), (022), (113), and (115) planes according to ICDD file 98-009-6856.

3.3. Optical analysis

Room-temperature spectral absorptivity/emissivity distributions of different samples are shown in Fig. 4. Due to the limits of the ranges between the two instruments (PerkinElmer Lambda 950 for UV–Vis, and SOC 100 for NIR-IR) as described in section 2.2 (Material characterizations and optical measurements), there is a slight discontinuity in every absorptivity/emissivity distribution curve at 2 μm. The absorptivity/emissivity difference between the two results measured by different instruments is more significant for Fiberfrax 140 than the other coating samples. The value for Fiberfrax 140 is almost 0.06, while the values for the other coatings are within 0.02. One reason can be used for explaining this difference is that Fiberfrax 140 is a porous material. Therefore, the size and the distribution of the micro cavities on the surface will lead to a strong influence on the spectra absorptivity distribution. Considering that the micro cavity distribution on the surface of the Fiberfrax 140 is not perfectly uniform and the illuminated areas of the two testing might be different, the deviation between these two results for the Fiberfrax 140 could be larger than the other coating samples.

In general, the optical performance of Fiberfrax 140 insulation material can be significantly changed and adapted for different applications by applying suited coatings on the surface. Furthermore, the trends in the spectral absorptivity distribution from all the coatings are similar with a significant absorptivity valley in the visible and near infrared spectrum (0.4 μm–2.5 μm) and relatively low absorptivity in natural solar irradiation spectrum with high thermal emissivity in the infrared region. The Al_2O_3 coated sample (Coating 1) excels in reflecting the radiative energy within the visible and near infrared bands (0.28 μm–2.2 μm). In the infrared spectrum (>0.7 μm), the absorptivity of the Fiberfrax 140 sample (Substrate material) is generally higher than other coatings. Upon comparing the spectral absorptivity curves of Coating 2 (MgO + Al_2O_3 = 1:1) and Coating 3 (MgO + Al_2O_3 = 2:1), we can conclude that the influence of the weight ratio in the spectral absorptivity distribution is negligible. Thus, considering the thermal stability performance results above, reducing the usage of MgO will be preferred.

For a qualitative estimation of the optical performance of the samples that we can expect in real solar applications, the normal solar absorptivity α_{sol} and the normal thermal emissivity $\varepsilon(T)$ were also calculated from the corresponding spectrum using Eq. (2) and Eq. (3) and the solar absorptivity are plotted Fig. 5. Among the six samples, the Fiberfrax 140 sample, coating 4 (100% MgO) and coating 5 (MgO + TiO_2 = 7:1) have relatively high solar absorptivity compared to Al_2O_3 coated sample (Coating 1) that shows the lowest solar absorptivity of 0.054. In other words, 94.6% solar irradiation can be reflected diffusely. This capability makes the Al_2O_3 coating an excellent solar reflector material in efficiently delivering the solar irradiation to the absorber in cavity receiver designs. Especially in the applications with strong solar light flux on the cavity wall, the other five materials will absorb at least two times more solar energy than the Al_2O_3 coating, leading to much higher temperatures.

Thermal emissivity results for the investigated samples are shown in Fig. 6. With the increase of the surface temperature, the peak of the spectral emissive power distribution moves towards the shorter wavelength side. Therefore, the trends of the thermal emissivity results are generally decreasing with the increase of the temperature. Fiberfrax 140 shows the highest thermal emissivity thus having the best ability in delivering the absorbed solar irradiation to the surrounding environment through thermal radiation. For the case when the cavity wall temperature is higher than the absorber temperature, this ability is helpful in managing the cavity wall temperature and redistributing the energy flux on the absorber. However, for cases where the cavity wall temperature is lower than the absorber temperature, lower thermal emissivity material is preferred. The sample with the second highest emissivity is coating 4 (100% MgO) with approximately 9% lower emissivity in the temperature range of 1073 K–1673 K. Between the other samples, the thermal emissivity differences are negligible (<2.5%) as shown in Fig. 6. By combining the results of the solar absorptivity and the thermal emissivity, the ε/α result can be obtained. In generally, it increases with the temperature for all the samples. Among all the 6 samples, coating 5 (MgO + TiO2 = 7:1) can offer highest ε/α value, and it can reach 0.73 at 1673 K. Therefore, comparing to other coatings, coating 5 is more suitable for the cavity receivers that the cavity temperature is higher than the absorber temperature according to conclusions achieved by Garrido et al. [29].

3.4. Surface morphology study

In addition to the chemical composition of the material itself, the surface microstructure of the material is also an important factor that strongly affects the optical properties of the material. Therefore, the LOM images of the Fiberfrax 140 sample and the 100% Al_2O_3 sample (Coating 1) together with their corresponding scanning electron

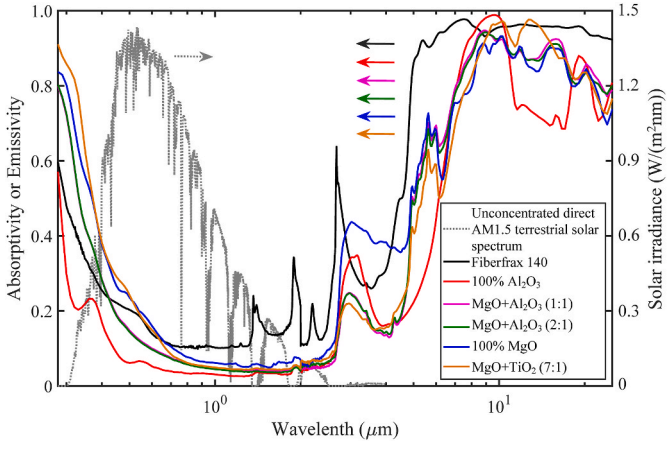

Fig. 4. Spectral absorptivity/emissivity distributions of the investigated samples.

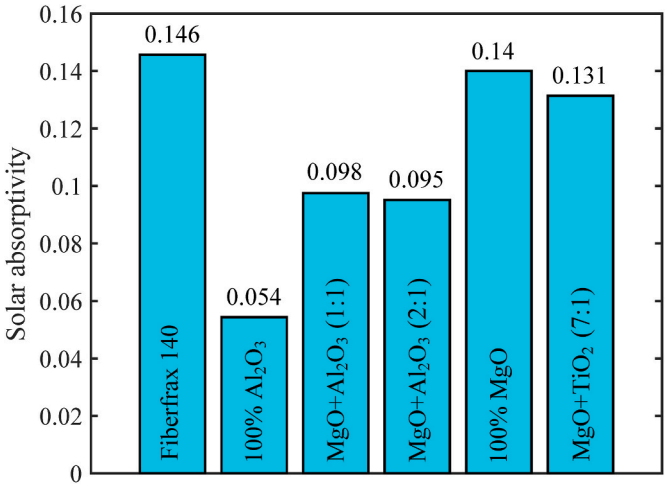

Fig. 5. Solar absorptivity results for the investigated samples.

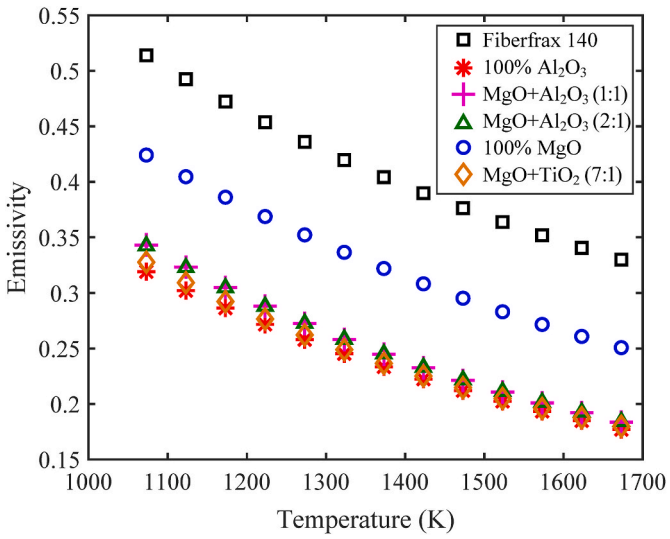

Fig. 6. Thermal emissivity results for the investigated samples.

micrographs (SEM) are presented in Fig. 7. In general, a flat surface will absorb less solar irradiation than the surface with micro cavities or porous surface that with the same surface material according to the theory of the radiation heat transfer [32]. Since the Fiberfrax 140 is an alumina-zirconia silica based refractory ceramic fiber material, the surface of the sample has a porous structure. The average size (>100 μm) of the micro pores on the surface is larger than the thermal infrared spectrum in the temperature range of this study by an order of magnitude, see Fig. 7(A) and (C), so these micro pores act as optical cavities that lead to significant enhancement in absorptivity/emissivity due to the cavity effect. Furthermore, the diameter of the fiber is close to the wavelength of the solar spectrum and the thermal infrared spectrum (see Fig. 7(C)), the scattering effect could also strongly affect the material optical properties. Unlike the Fiberfrax 140 substrate material, the Al_2O_3 coating has a relatively denser surface structure, see Fig. 7(B) and (D). Therefore, the cavity effect is minimized, and the surface optical properties are mainly depended on the coating material itself. Furthermore, the SEM result shows that the average size of the Al_2O_3 particle is still much larger than the wavelength range of 0.28–3 μm where the major energy of the solar irradiation located. Therefore, the geometric scattering will take the major optical phenomenon on the surface of the coating, and macroscopically form a diffuse reflective surface that is helpful in redistributing the solar irradiation uniformly on the absorber.

4. Conclusions

Five refractory solar selective reflector coatings have been prepared by painting metallic oxides on Fiberfrax 140 substrate (a commercial alumina-zirconia silica based refractory ceramic fiber material) with the help of commercial inorganic adhesives. Thermal stability testing has been conducted in a tubular furnace at a temperature of 1250 °C for 200 h under an ambient pressure with an airflow of 0.02 m/s. The optical performances have been studied by analyzing their spectral hemispherical reflectance in the spectrum band 0.25–25 μm with the help of lab spectrophotometers. Furthermore, the surface microstructure is also studied by using an optical microscope and a scanning electron microscopy. The following conclusions can be drawn:

(1). All the five coatings and the substrate material Fiberfrax 140 have good solar selective reflection characteristics: low solar absorptivity and relatively high thermal emissivity.
(2). The optical properties of the ceramic fiber-based cavity wall have been proved to be able to be adapted by metallic oxide coatings to

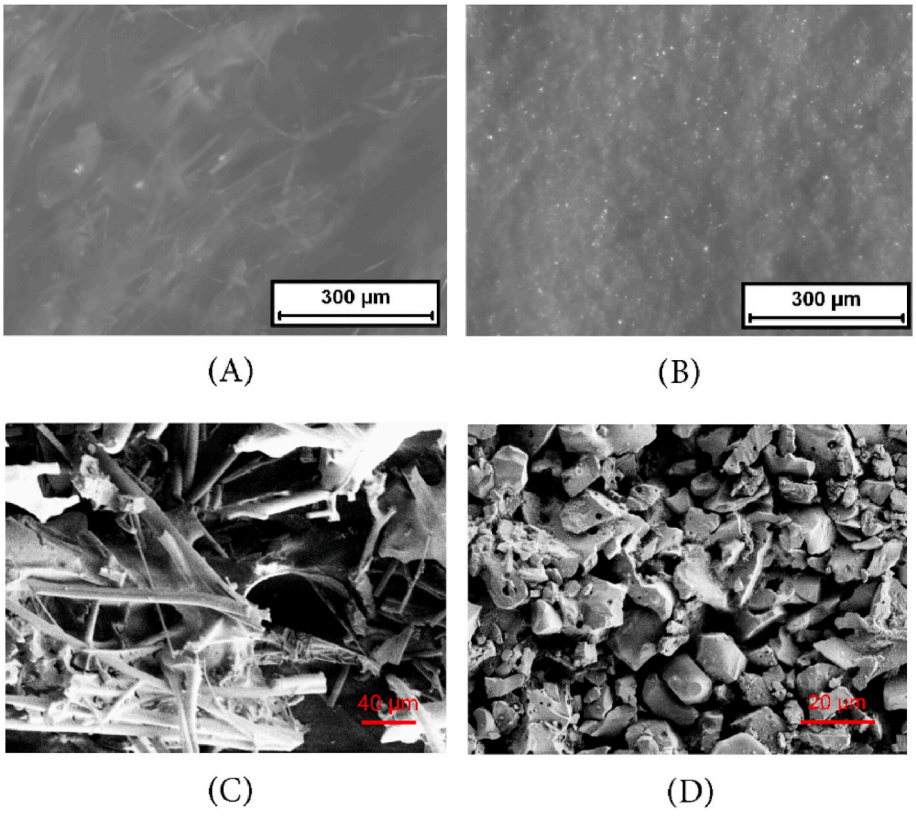

Fig. 7. Light optical microscope (LOM) images of (A) Fiberfrax 140 and (B) 100% Al_2O_3 coating, and their corresponding Scanning electron micrographs (SEM): (C) Fiberfrax 140 and (D) 100% Al_2O_3 coating.

meet various design requirements for maximizing the performance of cavity receivers.

(3). Among all the coatings, Al_2O_3 coating has the best performances both in thermal stability and solar selective reflection (94.6% in solar reflectivity).

(4). MgO has a negative effect on the thermal mechanical stability of the coating on Fiberfrax 140 substrate, and it is not recommended.

In the future, more these kind solar selective reflector coatings as well as substrate materials can be explored. Furthermore, considering the potential large-scale applications, spray-painting technology should be introduced for painting this coating on large-scale receiver for solar power tower systems.

CRediT authorship contribution statement

Wujun Wang: Conceptualization, Methodology, Resources, Investigation, Writing - original draft, Visualization. **Wangzhong Mu:** Resources, Investigation, Writing - review & editing. **Fei Ye:** Resources, Investigation, Writing - review & editing. **Silvia Trevisan:** Investigation, Writing - review & editing. **Joydeep Dutta:** Resources, Writing - review & editing, Supervision. **Björn Laumert:** Writing - review & editing, Funding acquisition, Supervision.

Declaration of competing interest

The authors declare that they have no known competing financial interests or personal relationships that could have appeared to influence the work reported in this paper.

Acknowledgements

This work was financially supported by Energimyndigheten (Project No. P46287-1). The authors also gratefully acknowledge Dr. Christophe Escape (CNRS PROMES) for his support in characterizing the surface optical properties.

References

[1] V.H. Dalvi, S.V. Panse, J.B. Joshi, Solar thermal technologies as a bridge from fossil fuels to renewables, Nat. Clim. Change 5 (2015) 1007–1013, https://doi.org/10.1038/nclimate2717.

[2] R. Pitz-Paal, Concentrating solar power: still small but learning fast, Nat. Energy. 2 (2017), https://doi.org/10.1038/nenergy.2017.95, 17095.

[3] K. Lovegrove, W. Stein, Concentrating solar power technology, Woodhead Publishing Limited (2012).

[4] G. Zhu, C. Libby, Review and future perspective of central receiver design and performance, AIP Conf. Proc. 1850 (2017), https://doi.org/10.1063/1.4984395.

[5] M. Mehos, C. Turchi, J. Vidal, M. Wagner, Z. Ma, C. Ho, W. Kolb, C. Andraka, Concentrating solar power Gen3 demonstration roadmap. https://doi.org/10.2172/1338899, 2017.

[6] M. Romero, A. Steinfeld, Concentrating solar thermal power and thermochemical fuels, Energy Environ. Sci. 9234 (2012) 5, https://doi.org/10.1039/c2ee21275g.

[7] L.A. Weinstein, J. Loomis, B. Bhatia, D.M. Bierman, E.N. Wang, G. Chen, Concentrating solar power, Chem. Rev. 115 (2015) 12797–12838, https://doi.org/10.1021/acs.chemrev.5b00397.

[8] W.H. Stein, R. Buck, Advanced power cycles for concentrated solar power, Sol. Energy 152 (2017) 91–105, https://doi.org/10.1016/j.solener.2017.04.054.

[9] I. Hischier, D. Hess, W. Lipinski, M. Modest, A. Steinfeld, Heat transfer analysis of a novel pressurized air receiver for concentrated solar power via combined cycles, J. Therm. Sci. Eng. Appl. 41002 (2009) 1, https://doi.org/10.1115/1.4001259.

[10] W. Wang, H. Xu, B. Laumert, T. Strand, An inverse design method for a cavity receiver used in solar dish Brayton system, Sol. Energy 110 (2014) 745–755, https://doi.org/10.1016/j.solener.2014.10.019.

[11] W. Wang, L. Fan, B. Laumert, A theoretical heat transfer analysis of different indirectly-irradiated receiver designs for high-temperature concentrating solar power applications, Renew, Energy 163 (2021) 1983–1993, https://doi.org/10.1016/j.renene.2020.10.113.

[12] W. Wang, B. Wang, L. Li, B. Laumert, T. Strand, The effect of the cooling nozzle arrangement to the thermal performance of a solar impinging receiver, Sol, Energy 131 (2016) 222–234, https://doi.org/10.1016/j.solener.2016.02.052.

[13] R. Korzynietz, J.A. Brioso, A. Río, M. Quero, M. Gallas, R. Uhlig, M. Ebert, R. Buck, D. Teraji, Solugas – comprehensive analysis of the solar hybrid Brayton plant, Sol. Energy 135 (2016) 578–589, https://doi.org/10.1016/j.solener.2016.06.020.

[14] P. Poživil, N. Ettlin, F. Stucker, A. Steinfeld, Modular design and experimental testing of a 50 kWth pressurized-air solar receiver for gas turbines, J. Sol. Energy Eng, 137 31002 (2015), https://doi.org/10.1115/1.4028918.

[15] D.G. Morris, A. López-Delgado, I. Padilla, M.A. Muñoz-Morris, Selection of high temperature materials for concentrated solar power systems: property maps and experiments, Sol. Energy 112 (2015) 246–258, https://doi.org/10.1016/j.solener.2014.09.050.

[16] T. Mancini, P. Heller, B. Butler, B. Osborn, W. Schiel, V. Goldberg, R. Buck, R. Diver, C. Andraka, J. Moreno, Dish-Stirling systems: an overview of development and status, J. Sol. Energy Eng 135 (2003) 125, https://doi.org/10.1115/1.1562634.

[17] R. Uhlig, B. Gobereit, J. Rheinländer, Advancing tube receiver performance by using corrugated tubes, Energy Procedia 69 (2015) 563–572, https://doi.org/10.1016/j.egypro.2015.03.065.

[18] W. Wang, B. Laumert, Effect of cavity surface material on the concentrated solar flux distribution for an impinging receiver, Sol. Energy Mater. Sol. Cells 161 (2017) 177–182, https://doi.org/10.1016/j.solmat.2016.12.008.

[19] J. Karni, Solar-thermal power generation, Annu. Rev. Heat Transf 15 (2012) 37–92.

[20] C.K. Ho, B.D. Iverson, Review of high-temperature central receiver designs for concentrating solar power, Renew. Sustain. Energy Rev. 29 (2014) 835–846, https://doi.org/10.1016/j.rser.2013.08.099.

[21] B.J. Hathaway, W. Lipiński, J.H. Davidson, Heat transfer in a solar cavity receiver: design considerations, Numer. Heat Transf, Part A Appl. 62 (2012) 445–461, https://doi.org/10.1080/10407782.2012.703471.

[22] M. Born, E. Wolf, Principles of Optics, sixth ed., Pergamon Press Ltd, 1980.

[23] M.F. Modest, Radiative Heat Transfer, second ed., Elsevier Science, New York, 2003.

[24] K.D. Olson, J.J. Talghader, Absorption to reflection transition in selective solar coatings, Optic Express 20 (2012) A554, https://doi.org/10.1364/OE.20.026744.

[25] C.E. Kennedy, Review of mid- to high- temperature solar selective absorber materials, Golden, Colorado (2002). https://www.nrel.gov/docs/fy02osti/31267.pdf.

[26] C. Atkinson, C.L. Sansom, H.J. Almond, C.P. Shaw, Coatings for concentrating solar systems – a review, Renew. Sustain. Energy Rev. 45 (2015) 113–122, https://doi.org/10.1016/j.rser.2015.01.015.

[27] F. Cao, K. McEnaney, G. Chen, Z. Ren, A review of cermet-based spectrally selective solar absorbers, Energy Environ. Sci, 7 1615 (2014), https://doi.org/10.1039/c3ee43825b.

[28] M. Ebert, W. Arnold, A. Avila-Marin, T. Denk, J. Hertel, A. Jensch, W. Reinalter, A. Schlierbach, R. Uhlig, Development of insulation for high flux density receivers, Energy Procedia 69 (2015) 369–378, https://doi.org/10.1016/j.egypro.2015.03.043.

[29] J. Garrido, L. Aichmayer, A. Abou-Taouk, B. Laumert, Experimental and numerical performance analyses of Dish-Stirling cavity receivers: radiative property study and design, Energy 169 (2019) 478–488, https://doi.org/10.1016/j.energy.2018.12.033.

[30] E.A. Fletcher, Solarthermal processing: a review, J. Sol. Energy eng 63 (2001) 123, https://doi.org/10.1115/1.1349552.

[31] Y.S. Touloukian, D.P. DeWitt, Thermal radiative properties: nonmetallic solids, Thermophysical Properties of Matter 8 (1972).

[32] F.P. Incropera, D.P. Dewitt, T.L. Bergman, A.S. Lavine, Fundamentals of Heat and Mass Transfer, sixth ed., John Wiley & Sons, 2007.

[33] J.A. Duffie, W.A. Beckman, Solar Engineering of Thermal Processes, fourth ed., John Wiley & Sons, New Jersey, 2013.

[34] C.A. Gueymard, D. Myers, K. Emery, Proposed reference irradiance spectra for solar energy systems testing, Sol. Energy 73 (2002) 443–467.